Tectonophysics 814 (2021) 228954

Contents lists available at ScienceDirect

Tectonophysics

journal homepage: www.elsevier.com/locate/tecto

The competing effects of olivine and orthopyroxene CPO on seismic anisotropy

Rachel E. Bernard [a,*,1], Vera Schulte-Pelkum [b], Whitney M. Behr [a,2]

[a] Department of Geological Sciences, Jackson School of Geosciences, The University of Texas at Austin, Austin, TX, United States of America
[b] Cooperative Institute for Research in Environmental Sciences and Department of Geological Sciences, University of Colorado Boulder, Boulder, CO, United States of America

A B S T R A C T

Orthopyroxene is the second most abundant mineral in the upper mantle and, like olivine, can form crystallographic preferred orientations (CPO) during mantle deformation that may influence mantle seismic anisotropy. Here we use a compilation of 21 peridotites in which both olivine and orthopyroxene CPOs are preserved to document the range of orthopyroxene CPO types and to explore their effects on seismic anisotropy of peridotites. In addition to four previously published orthopyroxene CPO types, this study establishes three new CPO types, two of which result in orthopyroxene fast axes aligned parallel to the lineation and the direction of mantle shear/flow. We calculate bulk elastic tensors for each sample from the measured olivine and orthopyroxene CPOs, and use those in turn to calculate Vp and Vs velocities and anisotropy percentages. In order to explore the relative influence of olivine and orthopyroxene on anisotropy, these properties were calculated for a range of possible modal percentages, from 100% olivine to 100% orthopyroxene. While the effect of orthopyroxene CPO appears to be a negligible influence on the orientation of bulk seismic fast axes, the presence of increasing orthopyroxene decreases the anisotropic signal overall. However, at very low olivine modal percentages, olivine and orthopyroxene can be mutually destructive, where the addition of olivine to a mostly orthopyroxene rock can actually decrease anisotropy.

1. Introduction

Elastically anisotropic minerals, when aligned, result in a directional dependence of P- and S-wave velocities. Propagating shear waves split into orthogonally polarized fast (S_1) and slow (S_2) components as a function of the elastic properties and elastic symmetry of these aligned minerals. The time delay between the arrival of fast and slow components, along with the azimuthal orientation of the fast shear wave, can be used to infer patterns of subsurface deformation (e.g. Silver, 1996; Savage, 1999; Long and Silver, 2009). This inference is dependent on assumptions as to what minerals are controlling this anisotropy, and how the minerals' axes align relative to the shear direction, or the direction of mantle flow.

It is well established that seismic anisotropy in the upper mantle is primarily due to the crystallographic preferred orientation (CPO) of olivine that forms typically from dislocation creep (e.g. Nicolas and Christensen, 1987; Karato et al., 2008; Long and Becker, 2010). The assumption that anisotropy is dominantly a reflection of olivine CPO – and not other upper mantle phases such as orthopyroxene, clinopyroxene, spinel, plagioclase, or garnet – is based on the observation that olivine is (1) the most abundant mineral at these depths and (2) the most inherently anisotropic. Most types of olivine CPO result in an alignment of the olivine fast axis ("a" or [100]) in the direction of flow. Therefore, in the mantle, fast axes are typically parallel to flow directions.

Orthopyroxene, while less anisotropic than olivine, also forms CPO from dislocation creep and is the second most abundant mineral in the upper mantle at around 20–30 modal percent (e.g. Ringwood, 1975). The most common orthopyroxene CPO type documented in past studies is characterized by an alignment of its slowest axes ("c" or [001]) in the direction of flow, as inferred from lineation (e.g. Christensen and Lundquist, 1982). While orthopyroxene CPO in this scenario would decrease the percentage of seismic anisotropy produced by olivine, it is not expected to affect the orientation of the seismic fast axes (e.g. Fischer et al., 2000; Blackman et al., 2002; Précigout and Almqvist, 2014).

The first aim of this paper is to catalog the various orthopyroxene CPO types that may exist in nature, using an extensive collection of peridotites from a variety of tectonic settings and localities. The second aim is to explore what, if any, effect these CPOs have on the seismic anisotropy of peridotites. This is critical because if orthopyroxene is shown to play a significant role in bulk peridotite anisotropy, it could

* Corresponding author.
E-mail address: rbernard@amherst.edu (R.E. Bernard).
[1] Present address: Department of Geology, Amherst College, Amherst, MA, United States of America.
[2] Present address: Geological Institute, Department of Earth Sciences, Swiss Federal Institute of Technology (ETH), Zurich, Switzerland.

https://doi.org/10.1016/j.tecto.2021.228954
Received 4 February 2021; Received in revised form 10 May 2021; Accepted 20 May 2021
Available online 5 June 2021

have important implications for how we interpret deformation or flow directions from seismic fast directions.

2. Methods and approach

Previous work used several naturally-deformed peridotites to invesitgate the relationship between olivine CPO type development and deformation conditions such as stress, water content, and temperature (Bernard et al., 2019). Of these 65 samples – which include xenoliths as well as peridotites from ophiolites and continental massifs all determined to have deformed through dislocation creep processes – 21 had identifiable orthopyroxene CPOs and are the focus of this study. These 21 samples, all of which are spinel peridotite xenoliths, come from San Carlos in Arizona, Kilbourne Hole in New Mexico, Cerro Chato locality of the central Rio Grande Rift (Byerly and Lassiter, 2012), Navajo Volcanic Field (Colorado Plateau) (Behr and Smith, 2016), Lunar Crater Volcanic Field in Nevada (Dygert et al., 2019), San Quintin Volcanic Field in Baja California Mexico, and the Cima Volcanic Field and Dish Hill localities of the Mojave region of southern California (Bernard and Behr, 2017). Additional information on all of these samples, as well as how thin sections were oriented using X-ray CT and the calculation of water contents from Secondary Ion Mass Spectrometry, can be found in Bernard et al. (2019).

2.1. Data acquisition

Electron Backscatter Diffraction (EBSD) data were collected on an ESEM XL30 at UT Austin to measure CPO in all phases of the peridotite samples. Polished thin sections were analyzed using 20–25 kV accelerating voltage, 15–20 mm working distance, medium to large spot size, 30–40× magnification, and 10–50 μm step sizes. Data were acquired using the Large Area Mapping tool in Oxford Instruments AZtec software (version 2.1). Postprocessing was conducted using the MTEX 4.4.0 toolbox developed for MATLAB (Bachmann et al., 2010; Mainprice et al., 2011). This code was used to create lower hemisphere equal area pole figures of the three principal axes in olivine and orthopyroxene: [100], [010], and [001]. These pole figures were used for the identification of CPO types. MTEX was also used to extract elastic tensor properties, analyze the seismic response of each sample, and calculate CPO fabric strengths using the M-index (Skemer et al., 2005) and J-index (Bunge, 1982). The M-index ranges from zero for a random CPO to 1 for a single crystal. The J-index ranges from 1 (random fabric) to infinity (single crystal).

2.2. Calculation of the elastic tensor and anisotropy parameters

The calculation of the effective elastic stiffness tensor, C, is critical for any calculation of anisotropy from CPO data. C is a fourth-order tensor that relates strain to stress for a given material. Using Voigt notation, anisotropic media can be expressed as a 6 × 6 matrix, C_{ij}, consisting of up to 21 independent coefficients, depending on the crystal symmetry (Voigt, 1928; Babuska and Cara, 1991). We calculated C_{ij} and seismic velocities through MTEX using built-in functions that take the experimentally-derived single crystal elastic tensors for olivine and orthopyroxene and create a single aggregate tensor based on the measured orientations of grains within the sample for defined olivine/orthopyroxene modal percents. We used Voigt-Reuss-Hill averaging, a well-established method that averages tensors derived from Voigt (assumes uniform strain) and Reuss (assumes uniform stress) approaches (Hill, 1952). We also used the single crystal elastic constants of Abramson et al. (1997) and Weidner et al. (1978) for olivine and for orthopyroxene, respectively. Tensors were generated for several user-defined modal percentages (rather than the true specimen modal percent), covering the range of all possible olivine-orthopyroxene contents. This was done in order to observe the influence of increasing amounts of orthopyroxene relative to olivine.

To quantify the relative influence of olivine and orthopyroxene on seismic anisotropy response, we use an approach similar to that of Ward et al. (2012), whose study looked at the competing effects of mica and quartz CPOs on the bulk seismic anisotropy of quartz-rich mylonites (their strategy was in turn similar to that of Tatham et al. (2008) and Lloyd et al. (2009)). Using the elastic tensor C_{ij}, we can use MTEX to calculate several measures of anisotropy, including the following (Mainprice and Silver, 1993):

- Compressional P-wave anisotropy percentage, **AVp**, as calculated by the equation $[(Vp_{max} - Vp_{min})/0.5(Vp_{max} + Vp_{min})] * 100$. This measurement characterizes the difference between minimum and maximum P-wave velocities (Vp) as a percentage of the mean.
- Shear wave splitting percentage, **AVs**, as calculated by the equation $[(Vs1 - Vs2)/0.5(Vs1 + Vs2)] * 100$ where Vs1 and Vs2 are the fast and slow shear wave velocities, respectively. This measurement is directionally dependent and characterizes the delay time between the fast and slow shear waves, which is relevant for anisotropic studies of shear wave splitting.
- Shear wave anisotropy percentage of the fast shear wave, **AVs1**, as calculated by $[(Vs1_{max} - Vs1_{min})/0.5(Vs1_{max} + Vs1_{min})] * 100$. This measurement characterizes the azimuthal variations of the fast shear wave.
- Shear wave anisotropy percentage of the slow shear wave, **AVs2**, as calculated by $[(Vs2_{max} - Vs2_{min})/0.5(Vs2_{max} + Vs2_{min})] * 100$. This measurement characterizes the azimuthal variations of the slow shear wave.

In order to explore the relative influence of olivine and orthopyroxene on the peridotites' overall anisotropy, we used MTEX to control the relative influence of each phase (i.e., imposing specific modal percentages) in calculating the elastic tensors and velocity parameters. For this exercise, we generated values and plots of AVp, AVs, and AVs1 for the following normalized ratios of olivine to orthopyroxene: 0/100, 20/80, 40/60, 60/40, 80/20, 100/0. In reality, the range of olivine-to-orthopyroxene in these samples – measured from modal percentages within the mapped areas and normalized to exclude other commonly present phases such as clinopyroxene and spinel – is 62/38 to 92/8 (Table 1).

3. Results and discussion

3.1. Orthopyroxene CPO types

Despite being the second most abundant mineral in the mantle, our current knowledge of orthopyroxene CPO is extremely limited (for a review see Jung, 2017). Experiments investigating the plastic deformation of orthopyroxene have found that (100)[001] slip is characteristic for this phase (Raleigh, 1965; Raleigh et al., 1971; Green and Radcliffe, 1972; Coe and Kirby, 1975; Ross and Nielsen, 1978). Less frequently, the slip systems (100)[010] and (010)[001] have also been observed experimentally (Raleigh et al., 1971; Ross and Nielsen, 1978; Naze, 1987; Ohuchi et al., 2011), with more recent experiments demonstrating that factors such as water content may affect active orthopyroxene slip systems (Manthilake et al., 2013).

The common (100)[001] slip system should result in a CPO characterized by the alignment of [100] axes normal to foliation and [001] axes parallel to the lineation. This CPO is indeed the most commonly documented, by far, for natural samples in the literature (Christensen and Lundquist, 1982; Vauchez and Garrido, 2001; Ishii and Sawaguchi, 2002; Vauchez et al., 2005; Skemer et al., 2006; Xu et al., 2006; Hidas et al., 2007; Falus et al., 2008; Tommasi et al., 2008; Skemer et al., 2010; Soustelle et al., 2010; Katayama et al., 2011; Satsukawa et al., 2011; Baptiste et al., 2012; Puelles et al., 2012; Chin et al., 2016; Demouchy et al., 2019; Liptai et al., 2019; Engvik et al., 2020). In fact, this CPO is considered to be so common that the orientation of orthopyroxene [100]

Table 1
CPO types for each sample, along with calculated values.

Sample	OL CPO	OPX CPO	Modal OL	Modal OPX	OL M-index	OL J-index	# OL grains	OPX M-Index	OPX J-Index	# OPX grains	OPX H2O ppm wt %
114027-10	E	ABC	74 (80)	18 (20)	0.18	3.87	364	0.06	3.41	112	94
114027-16	A	BA	74 (83)	15 (17)	0.13	3.24	350	0.11	3.39	149	–
114027-23	A	AB	64 (79)	17 (21)	0.11	3.00	278	0.14	4.17	102	11
116610-26	D	AC	66 (80)	16 (20)	0.11	2.71	475	0.05	2.24	200	184
117200-205	AG	AB	66 (78)	19 (22)	0.12	2.72	445	0.04	2.27	228	67
117200-211	AG	BC/ABC	54 (62)	33 (38)	0.22	4.62	264	0.13	3.59	135	–
CC07-1-22	C	CA	77 (87)	12 (13)	0.04	1.67	552	0.08	3.46	165	–
KH1	AG	BC	57 (73)	21 (27)	0.14	2.64	798	0.09	2.46	334	–
KH2	B	BC	45 (68)	21 (32)	0.08	2.23	395	0.03	2.19	174	174
N122	A	CB	75 (82)	17 (18)	0.23	5.52	492	0.28	7.51	169	–
N188	E	AB/AC	68 (75)	23 (25)	0.17	4.55	193	0.07	3.57	90	220
PL10	E	AC	86 (88)	12 (12)	0.09	3.02	1098	0.06	3.36	130	–
SQ2	D	CB	66 (79)	18 (21)	0.11	2.42	715	0.10	4.51	155	270
SQ3	D	CB	61 (74)	21 (26)	0.08	2.95	363	0.09	4.11	104	182
YFN11	E	CB	90 (91)	9 (9)	0.12	3.07	2592	0.11	4.18	275	34
YFN13	E	CB	55 (74)	19 (26)	0.07	1.93	842	0.25	17.26	85	82
RCiV8–22	A	BC	77 (92)	7 (8)	0.11	3.07	271	0.02	3.00	81	–
RDH23	E	CA	64 (81)	15 (19)	0.13	3.46	216	0.05	3.32	86	–
RDH33	D	CA	80 (84)	15 (16)	0.08	2.31	337	0.04	2.03	198	84
WCiVb46	E	CA	59 (76)	19 (24)	0.08	2.86	207	0.04	3.29	85	95
WCiVb47	A	CA	67 (71)	28 (29)	0.11	3.09	221	0.03	2.26	154	239

True modal percents of olivine and orthopyroxene are shown along with the normalized modal percentage between the two phases; the latter are shown in parentheses. M- and J- indices were calculated from EBSD data using MTEX, for a halfwidth of 10 degrees. The number of grains is indicative of the grains mapped and plotted from EBSD data. Water contents were obtained from SIMS and reported in Bernard et al. (2019); uncertainties were primarily due to heterogeneity of grains within each sample, which resulted in a standard error of ~15% of the reported averages. Information on localities also reported in Bernard et al. (2019). 114027- samples are from San Carlos, Arizona; 117200- and KH samples from Kilbourne Hole, New Mexico; CC07- from Cerro Chato, Rio Grande Rift; N122 and N188 from Navajo Volcanic Field, Colorado Plateau; PL10, YFN11, YFN13 from Lunar Crater Volcanic Field, Nevada; SQ samples from San Quintin Volcanic Field, Mexico; RCi- and WCi- from Cima Volcanic Field, Mojave; RDH- from Dish Hill, Mojave.

and [001] axes have been used as a reference frame for displaying CPO of other phases in samples where the lineation and/or foliation is unclear (that is, lineation is assumed to be parallel to orthopyroxene [001]) (Yu et al., 2019; Shao et al., 2021). However, some studies have also reported slip along the (010) glide plane (i.e. (010)[100] and/or (010)[001]) in naturally deformed orthopyroxene, often occurring along with (100)[001]) (Vauchez et al., 2005; Toy et al., 2010; Satsukawa et al., 2011; Baptiste et al., 2012; Chin et al., 2016).

A study by Jung et al. (2010) found the existence of four types of orthopyroxene CPO at a single peridotite xenolith locality. The authors of that study established a naming convention for orthopyroxene CPO types that we adopt here. This convention identifies types by slip systems – for example the common CPO caused by (100)[001] is known as "AC" because the a-axis is the slip plane and the c-axis is the slip direction. The three additional types of CPOs from Jung et al. (2010) are known as AB-type, BC-type, and ABC-type, which the authors found occurred as a function of orthopyroxene modal percent and water content (Fig. 1). In their study, AC-type was present in samples with lower orthopyroxene modal percent (<18%) and lower water contents than the other three types. In none of these previously reported CPO types does the fast orthopyroxene axis (the a-axis) align with the fast axis of olivine (also the a-axis). An exception is a study by Hidas et al. (2016), which described CPOs of orthopyroxene that mimicked that of olivine; however, in this case the observation was attributed to oriented synkinematic crystallization via dissolution–precipitation processes.

Our compilation reveals three additional orthopyroxene CPO types, which may be important for seismic anisotropy (Fig. 1). Using the same naming convention as Jung et al. (2010), we establish a CA-type (developed from the (001)[100] slip system), CB-type (the (001)[100] slip system), and BA-type (the (010)[100] slip system). The CA-type CPO is characterized by an alignment of the [100] axes in the lineation direction and [001] normal to foliation. It is identical to the olivine E-type CPO. The CB-type is characterized by [100] axes perpendicular to lineation within the foliation plane and [010] aligned parallel to lineation. The BA-type is identical to olivine A-type CPO, where the [100] axes are aligned parallel to lineation and [010] axes are normal to foliation. The CA-type and BA-type CPOs may be significant from a seismological standpoint, because the orthopyroxene fast axis is aligned parallel to the olivine fast axis, and as a result may not have the same destructive interference on anisotropy as the other types.

While the first to categorize them in this way, ours is not the first study to observe these unusual orthopyroxene CPOs. For example, Liu et al. (2019) found that a small number of peridotite xenoliths in their study preserved orthopyroxene CPOs similar to our BA- and CA-types. Prior workers on peridotite massifs have long noted the existence of orthopyroxene CPOs characterized by an alignment of the [001] axes parallel to lineation (as is the case for our CA- and CB-type); however, in all cases this abnormal orientation was interpreted as forming via dissolution-precipitation processes rather than dislocation creep (Suhr, 1993; Dijkstra et al., 2002; Hidas et al., 2016; Dilissen et al., 2018).

Of the 21 samples in this study, 5 had CA-type, 5 had CB-type, 3 had BC-type, 2 had AB-type, 2 had AC-type, 1 had ABC-type, and 1 had BA-type (Table 1). The remaining two samples had inconclusive CPO types appearing to be some combination of these. Orthopyroxene CPO M-indices range from 0.02 to 0.28, while J-indices range from 2.02 to 7.51 (excluding an outlier where the J-index was 17.26) (Table 1). Five samples (including the aforementioned outlier) have less than 100 grains of orthopyroxene mapped by EBSD, and therefore may have unreliable fabric strength indices (Table 1). More on these indicies can be found in the Appendix.

We find little evidence that there is a relationship between orthopyroxene CPO and its modal percent, as observed by Jung et al. (2010) (Table 1 and Fig. 2). Their study found that the AC-type samples had modal percentages <18%, while samples with AB-, BC-, and ABC-type CPO had higher modal percentages. In our dataset, the two AC-type samples indeed had low modal percentages (12–16%), but so did some BC- and AB-type samples. Modal percent seems less influential for the CPO types introduced in this study. We see a wide range of modal

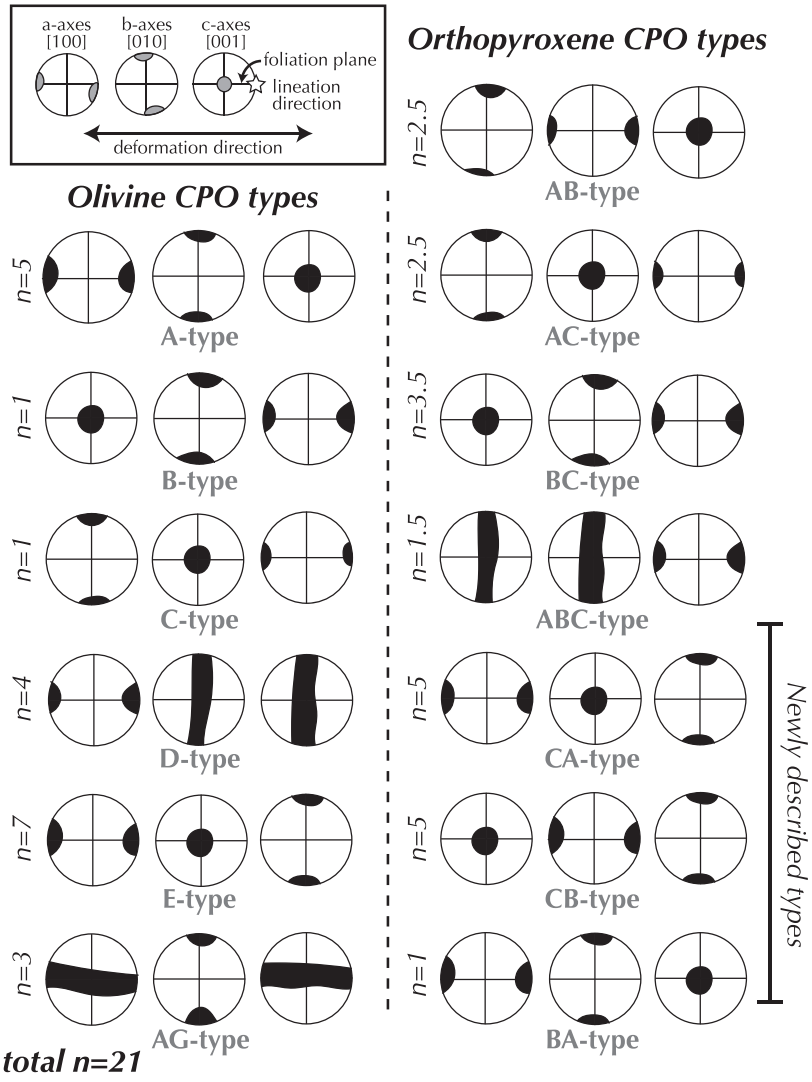

Fig. 1. Schematic pole figures showing the documented types of olivine and orthopyroxene CPO. The horizontal axis of each pole figure represents the foliation plane and lineation orientation. To the left of each CPO type is *n*, the number of samples in this study with that CPO type. Some orthopyroxene types have half numbers because two samples had a mixture of CPO types (see Table 1).

percentages among the samples with CA- and CB-type CPO (12–28% and 9–21%, respectively). The one sample with BA-type CPO had 15% orthopyroxene.

Finally, we investigated the relationship between orthopyroxene water content and CPO type (orthopyroxene water contents for 13 samples in this study were obtained through Secondary Ion Mass Spectrometry (SIMS) and reported in Bernard et al. (2019)). Unlike Jung et al. (2010), we find no evidence that AC-type is more common at lower water contents (Fig. 2). In fact, AB-type samples had the lowest water contents on average at 39 ppm H_2O wt% ($n = 2$); in comparison, the only AC-sample with measured orthopyroxene water contents contained 184 ppm H_2O wt% (Table 1).

3.2. Anisotropy trends with modal percentage

For the modal percent scenario where the olivine/orthopyroxene (Ol/Opx) ratio is 80/20, we find the following ranges for the aggregate: AVp: 4.84–10.90%; AVs: 4.20–7.74% (maximum); AVs1: 1.54–5.44%; AVs2: 0.73–6.05%; Vp: 7.88–8.10 km/s (minimum) to 8.50–8.91 km/s (maximum); Vs1: 4.75–4.90 km/s (minimum) to 4.95–5.06 km/s (maximum); Vs2: 4.62–4.74 km/s (minimum) to 4.77–4.91 km/s (maximum) (Supplementary Document Table S1). Unsurprisingly, the relative amounts of olivine and orthopyroxene have a significant effect on these values. Average trends over all samples, AVp, AVs (maximum), AVs1, and AVs2 all increase steadily with increasing olivine content (Figs. 3 and 4). The same is true for maximum Vs1 and Vp sample values. Maximum Vs2 decreases with increasing olivine content, as would be expected with increasing AVs. Modal percentage aside, there is a wide range of anisotropy parameters between samples, even for the case of pure orthopyroxene (Ol/Opx = 0/100) and pure olivine (Ol/Opx = 100/0) (Fig. 4). This variation is due to the variations in orthopyroxene and olivine CPO fabric strength.

Despite the multiple combinations of six olivine CPO types and seven orthopyroxene CPO types that exist in this dataset, some simple patterns emerge. For all samples – whether the orthopyroxene fast axis is parallel to that of olivine or not – the orientation of Vp and AVs anisotropy within the reference frame is determined solely by olivine when at least 20–40% of the sample is olivine. In other words, if a sample is 80%

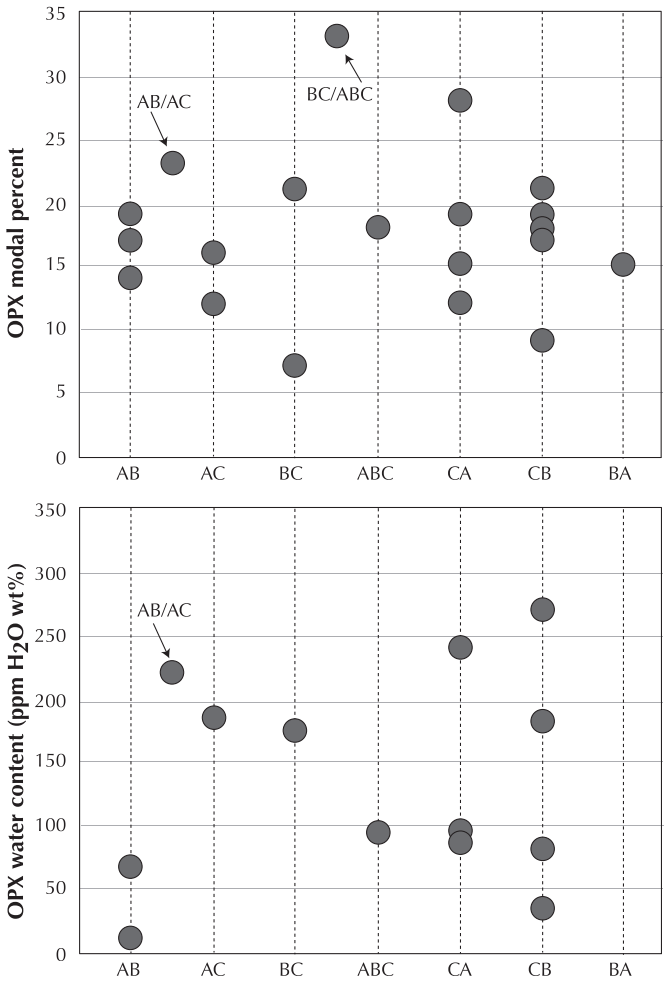

Fig. 2. Orthopyroxene modal percent and water content for individual samples, arranged by orthopyroxene CPO type.

orthopyroxene and 20% olivine, the orientation of the olivine CPO determines the bulk anisotropy. As an example, sample 117200-211 has an orthopyroxene CPO of BC/ABC-type and an olivine CPO of AG-type. In this sample, the [100] axis is arranged as a girdle within the foliation plane for olivine and normal to the foliation plane for orthopyroxene. When calculating Vp for a scenario when orthopyroxene is 100% of the sample, the fastest direction is normal to the foliation plane and lineation (the flow direction). When doing the same for the scenario when olivine is 100% of the sample, the fastest axis is within the foliation plane and subparallel to lineation. As shown in Fig. 3, at only 20% olivine (and 80% orthopyroxene), the fast axis is oriented within the foliation plane (Fig. 3 shows results for only one representative sample. Pole figures and anisotropy plots showing the same behavior can be found for the other samples in the Supplementary Document, Figs. S1 and S2). For all samples, this switch – where the bulk response reflects the olivine CPO – happens when olivine is 20–40% (Supplementary Document).

Also revealed by this dataset is confirmation that the presence of orthopyroxene decreases the overall anisotropy in all samples. Even when orthopyroxene's fast axes are oriented parallel to olivine's fast axes, it will decrease the intensity of seismic anisotropy because orthopyroxene is inherently less anisotropic. In general, increasing the proportion of olivine increases all measures of anisotropy (Fig. 4). In some samples, particularly those in which orthopyroxene and olivine fast axes are not subparallel, we see a decrease in anisotropy when olivine increases from 0 to 40 modal percent (Fig. 4). This is due to the mutually destructive nature of these CPOs, where the olivine and orthopyroxene fast axes cancel each other out. However, when olivine modal percent is above 40%, the addition of more olivine results in stronger anisotropy.

For typical mantle, olivine makes up more than 40%, so we can expect that despite the wide variety of orthopyroxene CPOs that exist in nature, anisotropy directions will reflect the CPO of olivine alone. However in settings with significant amounts of pyroxene, the wide array of orthopyroxene CPOs could result in complex patterns of anisotropy. While many pyroxenites only exist as veins, dykes, and layers within larger peridotite bodies (e.g. Wilshire et al., 1980; Garrido and Bodinier, 1999) and in quantities insignificant to large-scale seismic observations, there are geologic settings where a high proportion of orthopyroxene relative to olivine may be found in significant volumes. For example, the base of continental and intraoceanic arcs often contain excess amounts of pyroxenites resulting from processes such as crystal accumulation of mantle-derived magmas, interactions between peridotite and silicic melts generated from recycled oceanic crust, and metasomatism through silica enrichment (Ducea and Saleeby, 1998; Saleeby et al., 2003; Lee et al., 2006; Chin et al., 2014). Exposed sections of arcs have revealed layers of cumulate pyroxenites near paleo-Moho exposures that can be several km thick, as is the case in the Kohistan arc (Burg, 2011). Thermodynamic and crystal fractionation modeling efforts suggest these exposures considerably underestimate the original true thickness of these sections (Behn and Kelemen, 2006; Greene et al., 2006), as lower crustal foundering has likely removed signficant portions of this dense material (DeBari and Greene, 2011). For example, a reconstruction of the Talkeetna arc in Alaska, which has 500 m of pyroxenite section above the mantle exposure, suggests this arc once included a 10 km-thick section of pyroxenite (Hacker et al., 2008).

3.3. *Characterization of the elastic tensor*

Seismic observational and modeling studies rely on assumed elastic tensors. Characterizing the symmetry of elastic tensors collected from natural samples can inform these studies so that they best represent the complexities of nature. This suite of peridotites was used to compile a set of elastic tensors (Supplemntary Document Table S2) and observe how the modal percent and CPO of orthopyroxene affects the symmetry of these tensors using the decomposition approach of Browaeys and Chevrot (2004). In order of increasing symmetry and simplicity, the symmetry classes are triclinic (with 21 unique coefficients), monoclinic (13), orthorhombic (9), tetragonal (6), and hexagonal (5). Due to its simplicity, the hexagonal symmetry class is a typical assumption used for seismological studies of anisotropy both in the crust and mantle. Hexagonal symmetry refers to the case where there is a single fast or slow symmetry axis and isotropic velocities in the plane perpendicular to that axis. It is often referred to as transverse isotropy when the symmetry axis is vertical. While mantle anisotropy is fairly well approximated by fast-axis hexagonal symmetry (Becker et al., 2006), studies of natural samples have concluded that peridotites are best approximated instead by orthorhombic anisotropy (Schulte-Pelkum and Blackman, 2003; Worthington et al., 2013). It should be noted that the symmetry characterizing an elastic tensor derived from bulk alignment of minerals is not the same as the symmetry of a single mineral crystal (e.g., mica itself is a monoclinic mineral, but several micas together will align with one common axis in the direction of flow while the plane normal to flow is isotropic, displaying hexagonal anisotropy).

The original decomposition method paper of Browaeys and Chevrot (2004) showed results from one natural sample. The anisotropic component of that tensor was roughly 9% for only olivine, and 5% for a 70/30 mixture of olivine and orthopyroxene. In both scenarios, the largest anisotropic component was the hexagonal symmetry class, followed by orthorhombic and triclinic. The addition of orthopyroxene decreased the relative percentage of orthorhombic symmetry and added a small monoclinic component. The results of our study show that while this varies slightly from sample to sample, hexagonal symmetry

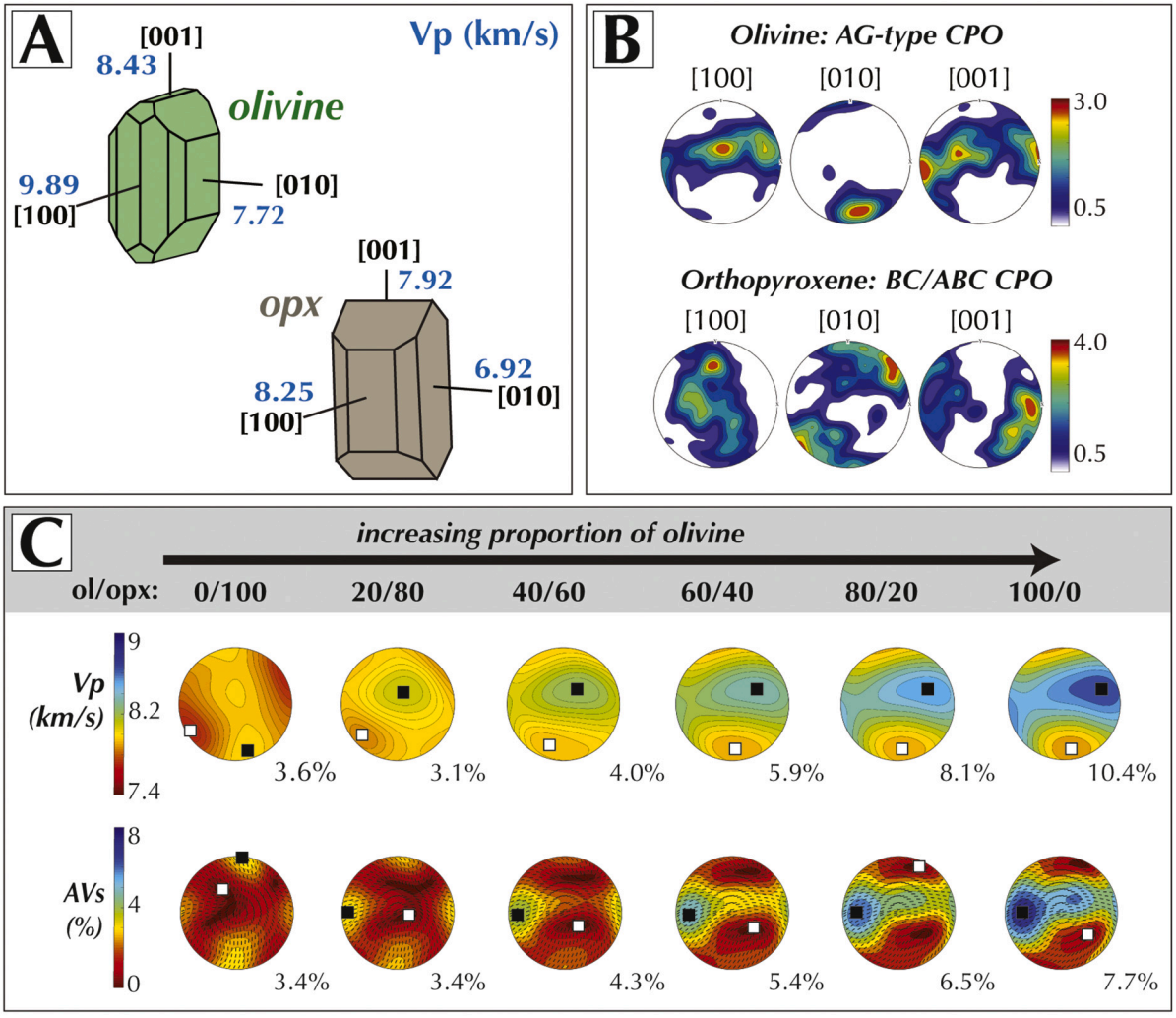

Fig. 3. A: Vp velocities for each olivine and orthopyroxene principal axis (Christensen, 1984). B: Equal area, lower hemisphere pole figures for olivine and orthopyroxene from sample 117200-211 (Kilbourne Hole). These contour plots are based on one point per grain, and plotted for a halfwidth of 10 degrees. Colorbar scales are an indication of pole figure strength (larger numbers equate to higher fabric strength). Number of grains plotted, M- and J-indices for this and other samples are listed in Table 1. C: (Top) Equal area lower hemisphere stereographic projections of Vp (km/s) calculated for a range of olivine and orthopyroxene modal percentages (with increasing normalized olivine percent moving left-to-right) for sample 117200-211. Maximum and minimum values indicated by black and white squares, respectively. Percentage anisotropy (AVp) included on bottom right of each spherical projection. (Bottom) Equal area lower hemisphere stereographic projects of AVs (%) calculated for the same modal percentages. Lines represent the trace of Vs1 polarization axes. Maximum AVs percent included on bottom right of each spherical projection.

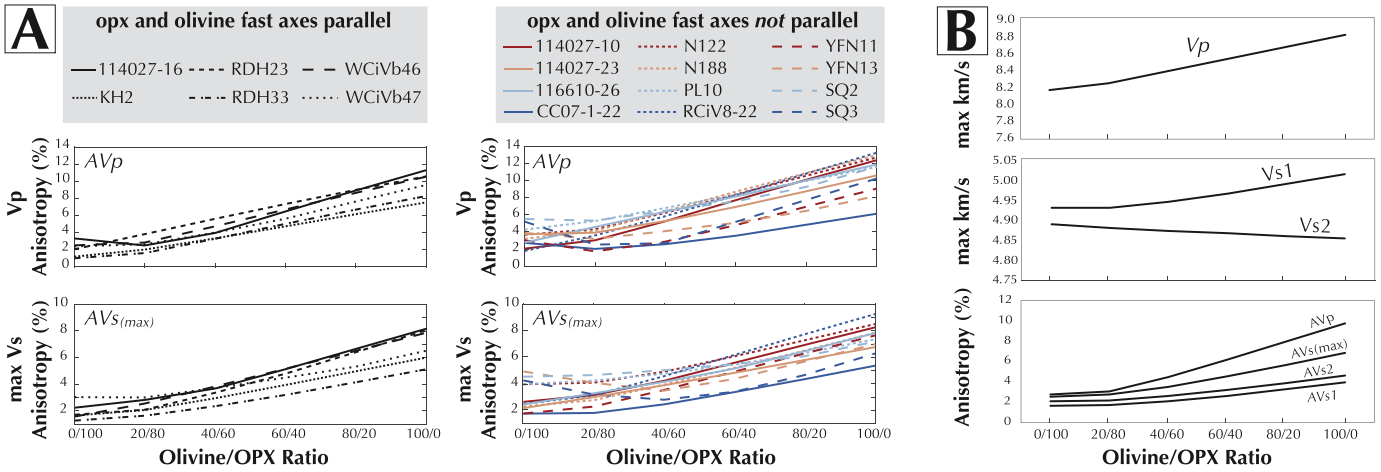

Fig. 4. A: Trends of AVp and maximum AVs percentages with increasing olivine content for (left) samples where the orthopyroxene and olivine fast axes are preferentially aligned similarly or (right) differently. Samples with girdled fast axes are not included. B: Trends of maximum Vp, Vs1, Vs2 (km/s) values, and AVp, maximum AVs, AVs1, and AVs2 percentages with increasing olivine content, averaged over all samples.

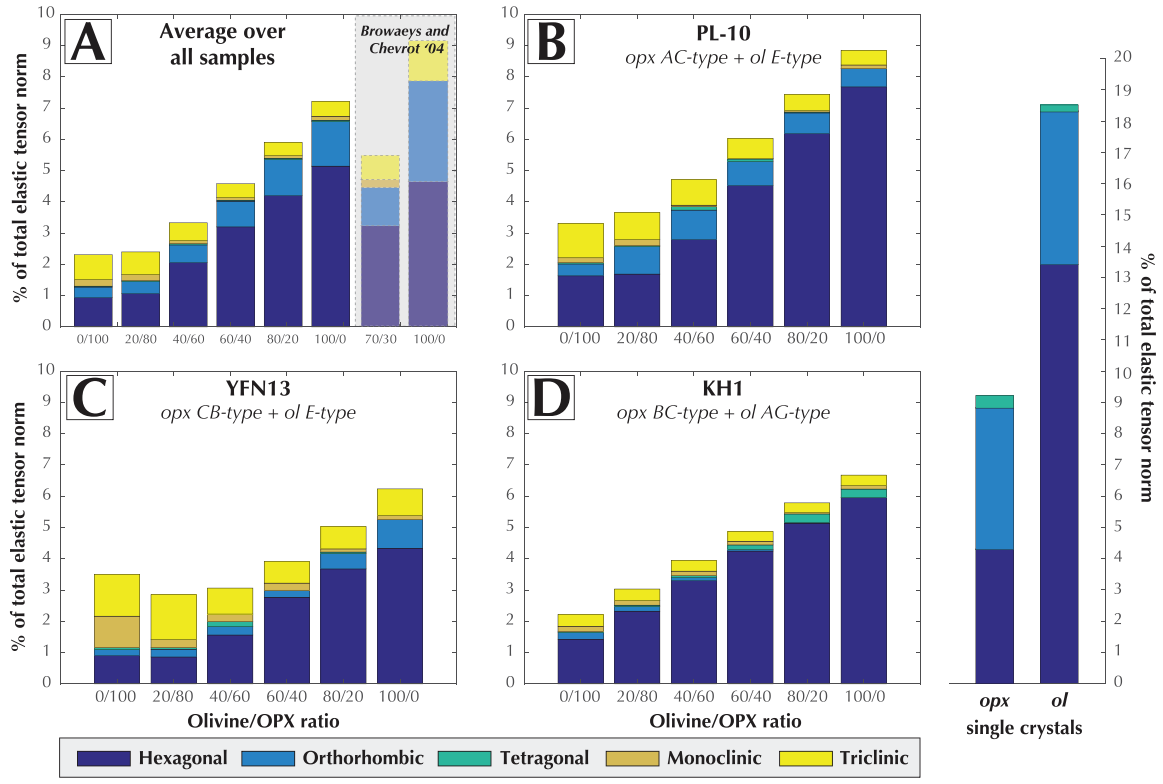

Fig. 5. Results from decomposition analysis where contributions of each symmetry class to the full tensor norm is represented as a percentage (the norm of each symmetry component vector divided by the full tensor norm). On the right, the decomposition results for single crystals of olivine and orthopyroxene (Abramson et al., 1997; Weidner et al., 1978). (A) Average decomposition breakdowns for all samples, averaged, shown alongside the results of a natural sample from Browaeys and Chevrot (2004). (B—D) Three individual samples showing variation between samples and consistent increase in the anisotropic component of the elastic tensor with increasing olivine content (left to right).

dominates the anisotropic component when olivine is greater than 20%. For the case of pure orthopyroxene, the anisotropic component is low (less than 3%) with roughly equal proportions of hexagonal and triclinic, along with smaller amounts of orthorhombic and monoclinic. We are most interested in the scenarios when olivine is greater than 60% of the tensor as is the case of the mantle. Here, we get very similar results to the representative natural sample of Browaeys and Chevrot (2004), where most of the tensor's anisotropic component is best approximated by hexagonal, followed by orthorhombic, then triclinic, and a small percentage of monoclinic symmetry. The presence of a monoclinic component in the 100% olivine scenario is perhaps the only difference between our average and their sample. Even the percent of the tensor that is anisotropic is remarkably similar. At 70% olivine, our anisotropic component would be extrapolated to almost exactly 5% of the tensor.

Because hexagonal symmetry is the largest proportion of the decomposition results, it would be sensible to conclude that hexagonal symmetry is the best approximation of these tensors. However, when we look at the decomposition results for a single crystal of olivine, we see that even here the approach of Browaeys and Chevrot (2004) give us a large hexagonal component, even though olivine itself is an orthorhombic mineral (Fig. 5). When looking at the CPOs as pole figures, we can see visually that many of our samples are clearly orthorhombic (e.g., those samples where we see point maxima rather than girdles) (Supplementary Document Fig. S1). This is an inherent feature of the decomposition approach; a symmetry that is clearly orthorhombic will still return large isotropic and hexagonal components because the lower symmetries are the deviations in the tensor norm from the higher symmetries. While the decomposition approach always returns a large hexagonal component, it still holds meaningful information regarding the influence of lower symmetry classes. On average, orthorhombic and lower symmetries comprise a larger percentage of the anisotropic portion of the tensor with increasing orthopyroxene content. There are interesting variations to these trends for some individual samples (Fig. 5). PL-10 – a peridotite with AC-type orthopyroxene CPO and olivine E-type CPO – had a relatively high proportion of anisotropy in its calculated tensor, which was almost entirely dominated by hexagonal symmetry at high olivine contents. YFN13 – a peridotite with CB-type orthopyroxene CPO and olivine E-type CPO – had a very large monoclinic component, particularly at high orthopyroxene contents. In both of these samples, there is also a small component of tetragonal symmetry, limited to the 40/60 olivine/orthopyroxene scenario. Finally, KH1 – a peridotite with BC-type orthopyroxene CPO and AG-type olivine CPO – was unique in that at high olivine contents, there was a significant tetragonal component and no orthorhombic component.

Again, despite the myriad of orthopyroxene and olivine CPO combinations, simple patterns emerge when looking at the dataset as a whole, particularly when focusing on the realistic scenario where the olivine/orthopyroxene ratio is 80/20. Looking at all samples in a ternary diagram that displays the fraction of hexagonal to orthorhombic to the remaining lower symmetry components (tetragonal + monoclinic + triclinic), it is evident that olivine and orthopyroxene CPO types do not appear to significantly affect the decomposition results (Fig. 6) (Brownlee et al., 2017). An exception might be olivine D-type CPO and orthopyroxene AC-type CPO, which consistently plot in the hexagonal corner of the diagram.

Also of interest to geophysicists is whether the best fit hexagonal tensor can best be approximated by fast or slow axis symmetry. Fast axis symmetry is typically assumed for the mantle, while slow axis symmetry

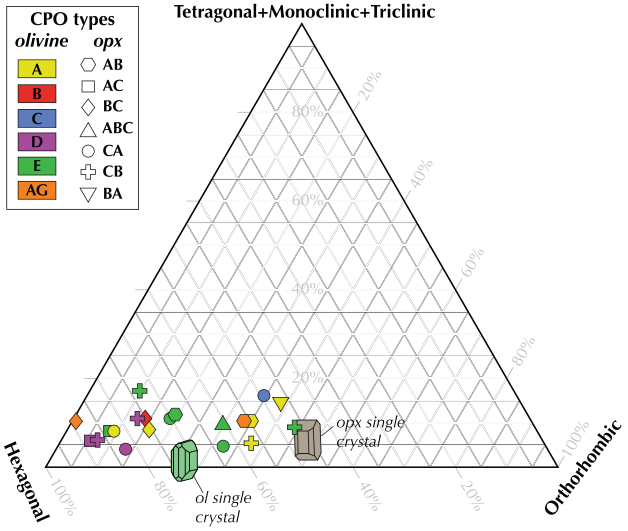

Fig. 6. Results from decomposition analysis showing fraction of hexagonal to orthorhombic to lower symmetry components (tetragonal + monoclinic + triclinic) for each sample, when the olivine/orthopyroxene ratio is 80/20. Also shown are the decomposition results for single crystals of olivine (Abramson et al., 1997) and orthopyroxene (Weidner et al., 1978).

is assumed for the crust (e.g. Brownlee et al., 2017). Different notation conventions exist for the five independent elastic parameters in the hexagonal case. One such convention is that of Love (1944), in which the five parameters are referred to as *A*, *C*, *F*, *L*, and *N*. Using the decomposition analysis, we extract the Love parameters and use them to determine whether the hexagonal component of the tensor is characterized by slow or fast axis symmetry; *C* is the symmetry axis constant and greater than *A* in the case of fast axis symmetry, and less than *A* in the case of slow axis symmetry. Overall, most samples have slow axis symmetry when the olivine/orthopyroxene ratio is 0/100 or 20/80, and fast axis symmetry when the olivine percentage is higher (Supplementary Document Fig. S2). While high olivine contents translate to fast axis symmetry in most cases, exceptions include the samples with olivine AG-type CPO, which is unsurprising as this CPO is characterized by an alignment of olivine's slowest axis [010] normal to the foliation plane with the other axes in a girdle within the foliation plane. A few samples classified as A-type – and the one B-type sample – also display slow axis symmetry at high olivine contents.

4. Conclusions and implications

The primary conclusions from this study are as follows:

1. In addition to the four previously published orthopyroxene CPO types, this study has revealed three new CPO types called CA-type, CB-type, and BA-type following the nomenclature of Jung et al. (2010). Of particular interest are CA- and BA-type, as they both result in the orthopyroxene fast axes [100] aligned in the direction of lineation, as is most common for olivine.
2. We see no evidence that variations of orthopyroxene CPO type are related to differing water contents or modal percentages.
3. Despite the wide variety of orthopyroxene CPO types – and the many combinations of orthopyroxene CPO and olivine CPO present in samples within this dataset – the CPO of orthopyroxene has no significant effect on overall seismic anisotropy when the olivine/orthopyroxene ratio is at least 40/60.
4. The addition of small amounts of olivine occasionally results in a temporary decrease in anisotropy from the 100% orthopyroxene scenario. In these cases – typically when the olivine and orthopyroxene fast axes are not aligned in the same direction – the orthopyroxene and olivine CPOs are mutually destructive. However above 40% modal olivine, Vp and Vs anisotropy always increases with increasing olivine content.

The implications of these findings are straightforward: at modal percentages common for most of the mantle (i.e. olivine >60%), the effect of orthopyroxene CPO is negligible on the orientation of seismic fast axes, although the presence of increasing orthopyroxene will decrease the overall anisotropic signal.

Key points

- Twenty-one peridotites from a variety of geological settings preserve seven orthopyroxene CPO types and six olivine CPO types.
- Despite many combinations of olivine and orthopyroxene CPOs, orthopyroxene has no significant effect on seismic anisotropy when olivine is at least 40% of the sample.
- Increasing orthopyroxene content decreases Vp and Vs anisotropy percentages.

A Supplementary data

Supplementary data to this article can be found online at https://doi.org/10.1016/j.tecto.2021.228954.

Declaration of competing interest

The authors declare that they have no known competing financial interests or personal relationships that could have appeared to influence the work reported in this paper.

Acknowledgments

We are grateful to S. Brownlee for her decomposition MATLAB script, and T. Becker, E. Chin, and two anonymous reviewers for feedback that improved this manuscript. This research was supported by a National Science Foundation (NSF) Graduate Research Fellowship made to R.E. Bernard and NSF grants EAR-1251621 awarded to W.M. Behr and EAR-1947765 to V. Schulte-Pelkum. We also thank J. Lassiter, D. Smith, the UT Austin Jackson School of Geosciences, and the Smithsonian National Museum of Natural History for loaning several samples. Data presented in this manuscript can be accessed through the Texas ScholarWorks repository (doi:10.15781/T2VQ2SW1G).

Appendix A. Quantifying CPO strength

Excluding an outlier with a J-index of 17.26, there appears to be a significant agreement ($R^2 = 0.80$) between J- and M-indices for orthopyroxene. This is only slightly less than the agreement between these indices for olivine ($R^2 = 0.84$). The M-index was originally developed and tested only for olivine, with the originators warning that it should only be used with similar materials with the same active slip systems (Skemer et al., 2005). The results of this study suggest that this index works as well for orthopyroxene as it does for olivine. While there does not appear to be a significant relationship between olivine CPO type and orthopyroxene CPO type, there is a moderate agreement between fabric strength of the two phases:

excluding the outlier sample, olivine versus orthopyroxene had a R^2 of 0.44 for J-index and 0.36 for M-index (Fig. A1). As observed in most studies of CPO in natural peridotite samples, olivine fabric strength is consistently higher than that of orthopyroxene, suggesting olivine accommodates more deformation than other phases. The positive relationship between olivine and orthopyroxene fabric strength suggests that like olivine, orthopyroxene fabric strength increases as a function of strain.

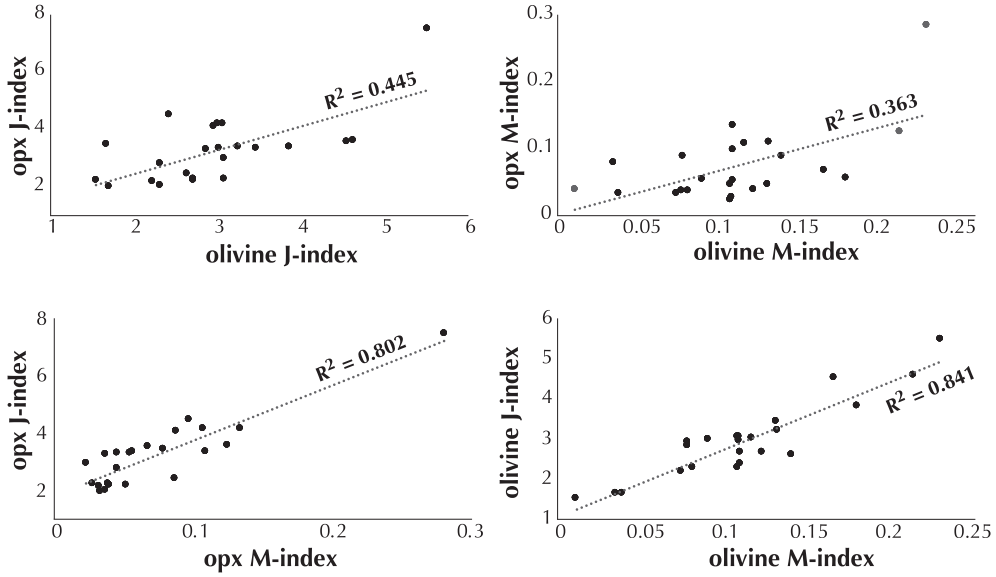

Fig. A1. Data and best fit line displaying the agreement of (top) fabric strength of olivine and orthopyroxene using the two fabric strength indices, and (bottom) fabric strength indices for each phase.

References

Abramson, E.H., Brown, J.M., Slutsky, L.J., Zaug, J., 1997. The elastic constants of San Carlos olivine to 17 GPa. J. Geophys. Res. 102 (B6), 12253–12263. https://doi.org/10.1029/97JB00682.

Babuska, V., Cara, M., 1991. Seismic Anisotropy in the Earth, 10th ed. Springer Science & Business Media.

Bachmann, F., Hielscher, R., Schaeben, H., 2010. Texture analysis with MTEX – free and open source software toolbox. Solid State Phenom. 160, 63–68. https://doi.org/10.4028/www.scientific.net/SSP.160.63.

Baptiste, V., Tommasi, A., Demouchy, S., 2012. Deformation and hydration of the lithospheric mantle beneath the Kaapvaal craton, South Africa. Lithos 149, 31–50. https://doi.org/10.1016/J.LITHOS.2012.05.001.

Becker, T.W., Chevrot, S., Schulte-Pelkum, V., Blackman, D.K., 2006. Statistical properties of seismic anisotropy predicted by upper mantle geodynamic models. J. Geophys. Res. 111 (B8), B08309 https://doi.org/10.1029/2005JB004095.

Behn, M.D., Kelemen, P.B., 2006. Stability of arc lower crust: Insights from the Talkeetna arc section, south Central Alaska, and the seismic structure of modern arcs. J. Geophys. Res. Solid Earth 111 (B11).

Behr, W.M., Smith, D., 2016. Deformation in the mantle wedge associated with Laramide flat-slab subduction. Geochem. Geophys. Geosyst. 17 (7), 2643–2660. https://doi.org/10.1002/2016GC006361.

Bernard, R.E., Behr, W.M., 2017. Fabric heterogeneity in the Mojave lower crust and lithospheric mantle in Southern California. J. Geophys. Res. Solid Earth 122 (7), 5000–5025. https://doi.org/10.1002/2017JB014280.

Bernard, R.E., Behr, W.M., Becker, T.W., Young, D.J., 2019. Relationships between olivine CPO and deformation parameters in naturally deformed rocks and implications for mantle seismic anisotropy. Geochem. Geophys. Geosyst. 20 (7), 3469–3494. https://doi.org/10.1029/2019GC008289.

Blackman, D.K., Wenk, H.-R., Kendall, J.M., 2002. Seismic anisotropy of the upper mantle 1. Factors that affect mineral texture and effective elastic properties. Geochem. Geophys. Geosyst. 3 (9), 1–24. https://doi.org/10.1029/2001GC000248.

Browaeys, J.T., Chevrot, S., 2004. Decomposition of the elastic tensor and geophysical applications. Geophys. J. Int. 159 (2), 667–678. https://doi.org/10.1111/j.1365-246X.2004.02415.x.

Brownlee, S.J., Schulte-Pelkum, V., Raju, A., Mahan, K., Condit, C., Orlandini, O.F., 2017. Characteristics of deep crustal seismic anisotropy from a compilation of rock elasticity tensors and their expression in receiver functions. Tectonics 36 (9), 1835–1857. https://doi.org/10.1002/2017TC004625.

Bunge, H.-J.H.J., 1982. Texture Analysis in Materials Science: Mathematical Methods. Butterworths, London.

Burg, J.-P., 2011. The Asia–Kohistan–India collision: Review and discussion. In: Arc-Continent Collision. Springer, pp. 279–309.

Byerly, B.L., Lassiter, J.C., 2012. Evidence from mantle xenoliths for lithosphere removal beneath the Central Rio Grande Rift. Earth Planet. Sci. Lett. 355–356, 82–93. https://doi.org/10.1016/J.EPSL.2012.08.034.

Chin, E.J., Lee, C.-T.A., Barnes, J.D., 2014. Thickening, refertilization, and the deep lithosphere filter in continental arcs: Constraints from major and trace elements and oxygen isotopes. Earth Planet. Sci. Lett. 397, 184–200.

Chin, E.J., Soustelle, V., Hirth, G., Saal, A.E., Kruckenberg, S.C., Eiler, J.M., 2016. Microstructural and geochemical constraints on the evolution of deep arc lithosphere. Geochem. Geophys. Geosyst. 17 (7), 2497–2521. https://doi.org/10.1002/2015GC006156.

Christensen, N.I., 1984. The magnitude, symmetry and origin of upper mantle anisotropy based on fabric analyses of ultramafic tectonites. Geophys. J. Int. 76 (1), 89–111.

Christensen, N.I., Lundquist, S.M., 1982. Pyroxene orientation within the upper mantle. Geol. Soc. Am. Bull. 93 (4), 279. https://doi.org/10.1130/0016-7606(1982)93<279:POWTUM>2.0.CO;2.

Coe, R.S., Kirby, S.H., 1975. The orthoenstatite to clinoenstatite transformation by shearing and reversion by annealing: Mechanism and potential applications. Contrib. Mineral. Petrol. 52 (1), 29–55. https://doi.org/10.1007/BF00378000.

DeBari, S.M., Greene, A.R., 2011. Vertical stratification of composition, density, and inferred magmatic processes in exposed arc crustal sections. In: Arccontinent Collision. Springer, pp. 121–144.

Demouchy, S., Tommasi, A., Ionov, D., Higgie, K., Carlson, R.W., 2019. Microstructures, water contents, and seismic properties of the mantle lithosphere beneath the northern limit of the Hangay Dome, Mongolia. Geochem. Geophys. Geosyst. 20 (1), 183–207. https://doi.org/10.1029/2018GC007931.

Dijkstra, A.H., Drury, M.R., Vissers, R.L., Newman, J., 2002. On the role of melt-rock reaction in mantle shear zone formation in the Othris Peridotite Massif (Greece). J. Struct. Geol. 24 (9), 1431–1450. https://doi.org/10.1016/S0191-8141(01)00142-0.

Dilissen, N., Hidas, K., Garrido, C.J., Kahl, W.-A., López Sánchez-Vizcaíno, V., Padron-Navarta, J.A., 2018. Textural evolution during high-pressure dehydration of serpentinite to peridotite and its relation to stress orientations and kinematics of subducting slabs: Insights from the Almirez ultramafic massif. Lithos 320-321, 470–489. https://doi.org/10.1016/j.lithos.2018.09.033.

Ducea, M.N., Saleeby, J.B., 1998. The age and origin of a thick mafic–ultramafic keel from beneath the Sierra Nevada batholith. Contrib. Mineral. Petrol. 133 (1), 169–185.

Dygert, N., Bernard, R.E., Behr, W.M., 2019. Great basin mantle xenoliths record active lithospheric downwelling beneath Central Nevada. Geochem. Geophys. Geosyst. 20 (2), 751–772.

Engvik, A.K., Mertens, C., Trepmann, C.A., 2020. Episodic deformation and reactions in mylonitic high-grade metamorphic granulites from Dronning Maud Land, Antarctica. J. Struct. Geol. 141, 104196. https://doi.org/10.1016/j.jsg.2020.104196.

Falus, G., Tommasi, A., Ingrin, J., Szabó, C., 2008. Deformation and seismic anisotropy of the lithospheric mantle in the southeastern Carpathians inferred from the study of mantle xenoliths. Earth Planet. Sci. Lett. 272 (1–2), 50–64. https://doi.org/10.1016/J.EPSL.2008.04.035.

Fischer, K.M., Parmentier, E.M., Stine, A.R., Wolf, E.R., 2000. Modeling anisotropy and plate-driven flow in the Tonga subduction zone back arc. J. Geophys. Res. Solid Earth 105 (B7), 16181–16191. https://doi.org/10.1029/1999JB900441.

Garrido, C.J., Bodinier, J.-L., 1999. Diversity of mafic rocks in the Ronda peridotite: evidence for pervasive melt–rock reaction during heating of subcontinental lithosphere by upwelling asthenosphere. J. Petrol. 40 (5), 729–754.
Green, H.W., Radcliffe, S.V., 1972. Deformation processes in the upper mantle. In: Flow and Fracture of Rocks, pp. 139–156. https://doi.org/10.1029/GM016p0139.
Greene, A.R., DeBARI, S.M., Kelemen, P.B., Blusztajn, J., Clift, P.D., 2006. A detailed geochemical study of island arc crust: the Talkeetna arc section, south-Central Alaska. J. Petrol. 47 (6), 1051–1093.
Hacker, B.R., Mehl, L., Kelemen, P.B., Rioux, M., Behn, M.D., Luffi, P., 2008. Reconstruction of the Talkeetna intraoceanic arc of Alaska through thermo-barometry. J. Geophys. Res. Solid Earth 113 (B3). https://doi.org/10.1029/2007JB005208.
Hidas, K., Falus, G., Szabó, C., Szabó, J., Kovács, I., Földes, T., 2007. Geodynamic implications of flattened tabular equigranular textured peridotites from the Bakony-Balaton Highland Volcanic Field (Western Hungary). J. Geodyn. 43 (43), 484–503. https://doi.org/10.1016/j.jog.2006.10.007.
Hidas, K., Tommasi, A., Garrido, C.J., Padrón-Navarta, J.A., Mainprice, D., Vauchez, A., Barou, F., Marchesi, C., 2016. Fluid-assisted strain localization in the shallow subcontinental lithospheric mantle. Lithos 262, 636–650. https://doi.org/10.1016/j.lithos.2016.07.038.
Hill, R., 1952. The elastic behaviour of a crystalline aggregate. Proc. Phys. Soc. Sec. A 65 (5), 349–354. https://doi.org/10.1088/0370-1298/65/5/307.
Ishii, K., Sawaguchi, T., 2002. Lattice- and shape-preferred orientation of orthopyroxene porphyroclasts in peridotites: an application of two-dimensional numerical modeling. J. Struct. Geol. 24 (3), 517–530. https://doi.org/10.1016/S0191-8141(01)00078-5.
Jung, H., 2017. Crystal preferred orientations of olivine, orthopyroxene, serpentine, chlorite, and amphibole, and implications for seismic anisotropy in subduction zones: a review. Geosci. J. 21 (6), 985–1011. https://doi.org/10.1007/s12303-017-0045-1.
Jung, H., Park, M., Jung, S., Lee, J., 2010. Lattice preferred orientation, water content, and seismic anisotropy of orthopyroxene. J. Earth Sci. 21 (5), 555–568. https://doi.org/10.1007/s12583-010-0118-9.
Karato, S.-I., Jung, H., Katayama, I., Skemer, P., 2008. Geodynamic significance of seismic anisotropy of the upper mantle: new insights from laboratory studies. Annu. Rev. Earth Planet. Sci. 36, 59–95.
Katayama, I., Michibayashi, K., Terao, R., Ando, J.-I., Komiya, T., 2011. Water content of the mantle xenoliths from Kimberley and implications for explaining textural variations in cratonic roots. Geol. J. 46 (2–3), 173–182. https://doi.org/10.1002/gj.1216.
Lee, C.-T.A., Cheng, X., Horodyskyj, U., 2006. The development and refinement of continental arcs by primary basaltic magmatism, garnet pyroxenite accumulation, basaltic recharge and delamination: insights from the Sierra Nevada, California. Contrib. Mineral. Petrol. 151 (2), 222–242.
Liptai, N., Hidas, K., Tommasi, A., Patkó, L., Kovács, I.J., Griffin, W.L., O'Reilly, S.Y., Pearson, N.J., Szabo, C., 2019. lateral and vertical heterogeneity in the lithospheric mantle at the northern margin of the Pannonian Basin reconstructed from peridotite xenolith microstructures. J. Geophys. Res. Solid Earth 124 (7), 6315–6336. https://doi.org/10.1029/2018JB016582.
Liu, S., Tommasi, A., Vauchez, A., Mazzucchelli, M., 2019. Crust-mantle coupling during continental convergence and break-up: constraints from peridotite xenoliths from the Borborema Province, Northeast Brazil. Tectonophysics 766, 249–269. https://doi.org/10.1016/j.tecto.2019.05.017.
Lloyd, G.E., Butler, R.W., Casey, M., Mainprice, D., 2009. Mica, deformation fabrics and the seismic properties of the continental crust. Earth Planet. Sci. Lett. 288 (1–2), 320–328. https://doi.org/10.1016/J.EPSL.2009.09.035.
Long, M.D., Becker, T.W., 2010. Mantle dynamics and seismic anisotropy. Earth Planet. Sci. Lett. 297, 341–354.
Long, M.D., Silver, P.G., 2009. Shear wave splitting and mantle anisotropy: Measurements, interpretations, and new directions. Surv. Geophys. 30 (4), 407–461.
Love, A.E.H., 1944. A Treatise on the Mathematical Theory of Elasticity, 4th ed. Dover Publications, New York.
Mainprice, D., Silver, P.G., 1993. Interpretation of SKS-waves using samples from the subcontinental lithosphere. Phys. Earth Planet. Inter. 78 (3–4), 257–280.
Mainprice, D., Hielscher, R., Schaeben, H., 2011. Calculating anisotropic physical properties from texture data using the MTEX open-source package. Geol. Soc. Lond., Spec. Publ. 360 (1), 175–192. https://doi.org/10.1144/SP360.10.
Manthilake, M.A.G.M., Miyajima, N., Heidelbach, F., Soustelle, V., Frost, D.J., 2013. The effect of aluminum and water on the development of deformation fabrics of orthopyroxene. Contrib. Mineral. Petrol. 165 (3), 495–505. https://doi.org/10.1007/s00410-012-0819-4.
Naze, L., 1987. TEM study of lattice defects in naturally and experimentally deformed orthopyroxenes. Bull. Mineral. 110, 497–512.
Nicolas, A., Christensen, N.I., 1987. Formation of anisotropy in upper mantle peridotites: a review. In: Fuchs, K., Froidevaux, C. (Eds.), Composition, Structure and Dynamics of the Lithosphere-Asthenosphere System. American Geophysical Union, Washington, D. C.
Ohuchi, T., Karato, S.-i., Fujino, K., 2011. Strength of single-crystal orthopyroxene under lithospheric conditions. Contrib. Mineral. Petrol. 161 (6), 961–975. https://doi.org/10.1007/s00410-010-0574-3.
Précigout, J., Almqvist, B.S.G., 2014. The Ronda peridotite (Spain): a natural template for seismic anisotropy in subduction wedges. Geophys. Res. Lett. 41 (24), 8752–8758. https://doi.org/10.1002/2014GL062547.
Puelles, P., Gil Ibarguchi, J.I., Beranoaguirre, A., Ábalos, B., 2012. Mantle wedge deformation recorded by high-temperature peridotite fabric superposition and hydrous retrogression (Limo massif, Cabo Ortegal, NW Spain). Int. J. Earth Sci. 101 (7), 1835–1853. https://doi.org/10.1007/s00531-012-0761-8.
Raleigh, C., 1965. Reports glide mechanisms in experimentally deformed minerals. Science 150, 739–741.
Raleigh, C., Kirby, S.H., Carter, N.L., Lallemant, H.G.A., 1971. Slip and the clinoenstatite transformation as competing rate processes in enstatite. J. Geophys. Res. 76 (17), 4011–4022. https://doi.org/10.1029/JB076i017p04011.
Ringwood, A.E., 1975. Composition and Petrology of the Earth's Mantle, 618.
Ross, J.V., Nielsen, K., 1978. High-temperature flow of wet polycrystalline enstatite. Tectonophysics 44 (1–4), 233–261. https://doi.org/10.1016/0040-1951(78)90072-0.
Saleeby, J., Ducea, M., Clemens-Knott, D., 2003. Production and loss of high-density batholithic root, southern Sierra Nevada, California. Tectonics 22 (6).
Satsukawa, T., Michibayashi, K., Anthony, E.Y., Stern, R.J., Gao, S.S., Liu, K.H., 2011. Seismic anisotropy of the uppermost mantle beneath the Rio Grande rift: evidence from Kilbourne Hole peridotite xenoliths, New Mexico. Earth Planet. Sci. Lett. 311, 172–181.
Savage, M., 1999. Seismic anisotropy and mantle deformation: what have we learned from shear wave splitting? Rev. Geophys. 37 (1), 65–106.
Schulte-Pelkum, V., Blackman, D.K., 2003. A synthesis of seismic P and S anisotropy. Geophys. J. Int. 154 (1), 166–178. https://doi.org/10.1046/j.1365-246X.2003.01951.x.
Shao, Y., Prior, D.J., Scott, J.M., Negrini, M., 2021. Pre-Alpine Fault fabrics in mantle xenoliths from East Otago, South Island, New Zealand. J. Geophys. Res. Solid Earth. https://doi.org/10.1029/2020JB020196.
Silver, P.G., 1996. Seismic anisotropy beneath the continents: probing the depths of geology. Annu. Rev. Earth Planet. Sci. 24 (1), 385–432. https://doi.org/10.1146/annurev.earth.24.1.385.
Skemer, P., Katayama, I., Jiang, Z., Karato, S.-I., 2005. The misorientation index: development of a new method for calculating the strength of lattice-preferred orientation. Tectonophysics 411 (1–4), 157–167. https://doi.org/10.1016/j.tecto.2005.08.023.
Skemer, P., Katayama, I., Karato, S.-i., 2006. Deformation fabrics of the Cima di Gagnone peridotite massif, Central Alps, Switzerland: evidence of deformation at low temperatures in the presence of water. Contrib. Mineral. Petrol. 152 (1), 43–51. https://doi.org/10.1007/s00410-006-0093-4.
Skemer, P., Warren, J.M., Kelemen, P.B., Hirth, G., 2010. Microstructural and rheological evolution of a mantle shear zone. J. Petrol. 51 (1–2), 43–53. https://doi.org/10.1093/petrology/egp057.
Soustelle, V., Tommasi, A., Demouchy, S., Ionov, D.A., 2010. deformation and fluid-rock interaction in the supra-subduction mantle: microstructures and water contents in peridotite xenoliths from the Avacha Volcano, Kamchatka. J. Petrol. 51 (1–2), 363–394. https://doi.org/10.1093/petrology/egp085.
Suhr, G., 1993. Evaluation of upper mantle microstructures in the Table Mountain massif (Bay of Islands ophiolite). J. Struct. Geol. 15 (11), 1273–1292. https://doi.org/10.1016/0191-8141(93)90102-G.
Tatham, D., Lloyd, G., Butler, R., Casey, M., 2008. Amphibole and lower crustal seismic properties. Earth Planet. Sci. Lett. 267 (1–2), 118–128. https://doi.org/10.1016/J.EPSL.2007.11.042.
Tommasi, A., Vauchez, A., Ionov, D., 2008. Deformation, static recrystallization, and reactive melt transport in shallow subcontinental mantle xenoliths (Tok Cenozoic volcanic field, SE Siberia). Earth Planet. Sci. Lett. 272, 65–77. https://doi.org/10.1016/j.epsl.2008.04.020.
Toy, V.G., Newman, J., Lamb, W., Tikoff, B., 2010. The role of pyroxenites in formation of shear instabilities in the mantle: evidence from an ultramafic ultramylonite, Twin Sisters Massif, Washington. J. Petrol. 51 (1–2), 55–80. https://doi.org/10.1093/petrology/egp059.
Vauchez, A., Garrido, C.J., 2001. Seismic properties of an asthenospherized lithospheric mantle: constraints from lattice preferred orientations in peridotite from the Ronda massif. Earth Planet. Sci. Lett. 192, 235–249.
Vauchez, A., Dineur, F., Rudnick, R., 2005. Microstructure, texture and seismic anisotropy of the lithospheric mantle above a mantle plume: insights from the Labait volcano xenoliths (Tanzania). Earth Planet. Sci. Lett. 232 (3–4), 295–314. https://doi.org/10.1016/J.EPSL.2005.01.024.
Voigt, W., 1928. Lehrbuch der Kristallphysik (mit Ausschluss der Kristalloptik). Springer-Verlag.
Ward, D., Mahan, K., Schulte-Pelkum, V., 2012. Roles of quartz and mica in seismic anisotropy of mylonites. Geophys. J. Int. 190 (2), 1123–1134. https://doi.org/10.1111/j.1365-246X.2012.05528.x.
Weidner, D.J., Wang, H., Ito, J., 1978. Elasticity of orthoenstatite. Phys. Earth Planet. Inter. 17 (2), P7–P13. https://doi.org/10.1016/0031-9201(78) 90043-2.
Wilshire, H.G., Pike, J.N., Meyer, C.E., Schwarzman, E.C., 1980. Amphibole-rich veins in lherzolite xenoliths, Dish Hill and Deadman Lake, California. Am. J. Sci. A 280, 576–593.
Worthington, J.R., Hacker, B.R., Zandt, G., 2013. Distinguishing eclogite from peridotite: EBSD-based calculations of seismic velocities. Geophys. J. Int. 193 (1), 489–505. https://doi.org/10.1093/gji/ggt004.
Xu, Z., Wang, Q., Ji, S., Chen, J., Zeng, L., Yang, J., Chen, F., Liang, F., Wenk, H.-R., 2006. Petrofabrics and seismic properties of garnet peridotite from the UHP Sulu terrane (China): Implications for olivine deformation mechanism in a cold and dry subducting continental slab. Tectonophysics 421 (1–2), 111–127. https://doi.org/10.1016/J.TECTO.2006.04.010.
Yu, M., Wang, Q., Yang, J., 2019. Fabrics and water contents of peridotites in the Neotethyan Luobusa ophiolite, southern Tibet: implications for mantle recycling in supra-subduction zones. J. Geol. Soc. 176 (5), 975–991. https://doi.org/10.1144/jgs2018-152.